Received 25 June 2026; accepted 26 July 2026. Date of publication 4 August 2026;
date of current version 12 August 2026. The review of this article was arranged by Associate Editor Yongchang Zhang.

Digital Object Identifier 10.1109/OJPEL.2026.3719597

Weighting-Factor-Free Sequential Predictive Torque Control Using Virtual Vectors in Six-Phase IM

PAOLA MAIDANA [1], CHRISTIAN MEDINA [1], JESÚS DOVAL-GANDOY [2] (Member, IEEE), JORGE RODAS [1] (Senior Member, IEEE), OSVALDO GONZALEZ [1], MAGNO AYALA [1] (Member, IEEE), AND RAUL GREGOR [1] (Member, IEEE)

[1]CITHED, Department of Electronic and Mechatronic Engineering, Facultad de Ingeniería, Universidad Nacional de Asunción, Luque 110948, Paraguay
[2]Applied Power Electronics Technology Research Group, CINTECX, Universidad de Vigo, 36310 Vigo, Spain

CORRESPONDING AUTHOR: PAOLA MAIDANA (e-mail: pmaidana@fiuna.edu.py)

This work was supported in part by Facultad de Ingeniería, Universidad Nacional de Asunción (FIUNA), Paraguay, in part by Consejo Nacional de Ciencia y Tecnología (CONACYT), Paraguay, through Programa de Incentivos para la Formación de Investigadores en Posgrados Nacionales under Grant BCAS02, in part by SISNI Program, in part by Project ESTR01-3, Project PINV02-191, and Project PINV01-272, in part by the Government of Galicia under Grant GPC-ED431B 2023/12, in part by Spanish State Research Agency (AEI) under Project PID2022-136908OB-I00 (MCIN/AEI/10.13039/501100011033/FEDER-UE), and in part by Thematic Network RIBIERSE-CYTED under Grant 723RT0150.

ABSTRACT Finite-control-set model predictive torque control of multiphase induction machines is often limited by heuristic tuning of weighting factors and inadequate secondary-plane current regulation. To address these limitations, this paper proposes a weighting-factor-free sequential model predictive torque control strategy with virtual voltage vector synthesis (SMPTC-VV) for six-phase induction machine drives supplied by dual two-level voltage source inverters. The proposed scheme employs a sequential optimisation structure that removes weighting factors from the cost function formulation. Virtual voltage vectors are incorporated to suppress non-torque-producing currents in the $x-y$ plane, enabling simultaneous regulation of electromagnetic torque, stator flux, and secondary-plane currents. Experimental validation under steady-state and dynamic conditions, including $\pm 25\%$ magnetising inductance mismatch, demonstrates accurate torque and flux regulation, fast transient response, and improved current quality. The proposed strategy achieves improvements of 10.08% and 53.41% in THD_{α}, and 54.26% and 69.21% in THD_{a}, compared to SMPTC and classical PTC, respectively. In addition, flux regulation is improved by 28.03% and 31.13% relative to SMPTC and classical PTC, respectively, while non-torque-producing $x-y$ currents are improved by 75.40% and 82.58% with respect to SMPTC and classical PTC. The computational effort is limited to 966 floating-point operations per sampling period, corresponding to improvements of 50.66% and 75.66% relative to SMPTC and classical PTC, respectively. The results demonstrate an efficient and experimentally validated predictive torque control solution for high-performance multiphase drives.

INDEX TERMS Multiphase IM, sequential model predictive torque control, six-phase drives, virtual voltage vectors.

I. INTRODUCTION

Model predictive control (MPC) is an advanced control strategy that relies on mathematical models of the system to predict future behaviour of the controlled variables and determine actuation signals. MPC is generally classified into two main categories: continuous-control-set MPC and finite-control-set MPC (FCS-MPC). The former requires a modulation stage, which typically increases the overall algorithmic complexity. The latter exhibits an intuitive structure, a straightforward implementation, and effectively addresses nonlinearities and multivariable control issues [1]. These features make FCS-MPC well-suited for applications in power electronics and electric drives.

Typical applications of FCS-MPC include energy management in DC microgrids and hybrid energy storage systems, where fast power balancing and handling of constraints are required [2]. The approach has also been applied in renewable energy conversion systems, such as photovoltaic and wind power interfaces, which demand flexible active and reactive power control with fast transient response [3]. In electric drive applications, FCS-MPC has been widely employed in machine drives fed by parallel converters, where multirate prediction and structured switching-state selection strategies have been introduced to mitigate circulating currents, enhance dynamic performance, and improve computational efficiency [4].

From an implementation perspective, at each sampling instant, FCS-MPC evaluates a finite set of candidate control actions and selects the one that minimises a predefined cost function. This function reflects the desired system behaviour by penalising tracking errors while enforcing system constraints [5]. Consequently, multiple control objectives are typically aggregated within a weighted formulation. A key challenge is therefore the appropriate selection of the weighting factor (WF) [6]. To tackle this issue, the methods reported in the literature can be broadly classified into two categories: (i) WF selection strategies and (ii) WF elimination approaches.

Within the first category, numerous strategies for selecting WF have been proposed. For instance, optimisation-based approaches have been reported to select the WF by balancing torque ripple and stator current distortion [7]. In addition, learning-based techniques have been employed to determine suitable cost-function parameters under varying operating conditions, including artificial neural networks [8] and deep residual networks with dynamic tuning [9]. Furthermore, multiobjective optimisation methods based on particle swarm optimisation and Pareto dominance concepts have been proposed to provide systematic offline WF tuning for predictive current control of electric drives [10]. Nevertheless, because no universally applicable systematic formulation is available, WF selection remains strongly dependent on operating conditions and design trade-offs. Consequently, its adjustment often relies on empirical procedures, which increase design complexity.

To address these issues, WF elimination has been proposed using various strategies in the literature [11]. One approach relies on homogeneous control variables, where heterogeneous objectives are reformulated into a single physical quantity. An illustrative example is given in [12], where predictive torque control (PTC) is replaced by predictive flux control. Geometric reformulation methods, such as those described in [13], compute a required voltage vector and select the nearest switching state, avoiding the explicit use of a multi-term cost function. Alternatively, in [14], a cascaded predictive structure eliminates the need for WF by hierarchical loop separation, thereby regulating different objectives across distinct predictive stages. However, in these approaches, either the multi-objective nature of the problem is simplified, or objective prioritisation remains implicitly embedded in the formulation or architecture. In contrast, sequential model predictive control (SMPC), as proposed in [15], establishes a formally structured optimisation hierarchy within a single predictive scheme, preserving the multi-objective formulation, avoiding heuristic WFs, and reducing computational burden, thereby facilitating real-time implementation in electric drive applications.

In parallel with the development of advanced control strategies, electric drive system architectures have evolved significantly to meet increasingly stringent requirements for reliability, power distribution, and overall system performance. In this context, conventional drive systems based on three-phase machines have been widely adopted for decades but exhibit inherent limitations when deployed in critical applications that demand high operational availability and enhanced fault tolerance, such as electric vehicles, marine propulsion systems, and aerospace applications [16], [17], [18].

In response to these limitations, drive systems based on multiphase machines ($n > 3$) have attracted growing interest in both academic and industrial communities, primarily because they can reduce phase current, improve the harmonic profile of the electromagnetic torque, and introduce structural redundancy, enabling operation under fault conditions with controlled performance degradation [19]. However, increasing the number of phases inherently complicates modelling and control tasks, primarily because additional orthogonal planes appear in the vector representation of electrical variables, such as the $x - y$ plane [20].

In the early stages of multiphase drive development, control strategies were largely derived from direct extensions of classical control schemes originally developed for three-phase machines. Among these, field-oriented control (FOC) and direct torque control (DTC) have been widely applied to IM drives [21], [22], [23]. In FOC-based approaches, pulse-width modulation and proportional–integral controllers are employed to achieve decoupled regulation of flux and torque, while enabling simultaneous current regulation in both the main and secondary-planes. Conversely, DTC directly regulates torque and flux through hysteresis controllers and predefined switching tables. However, this approach is typically associated with increased torque ripple. More generally, the multi-objective nature of multiphase drive control poses significant challenges for conventional control strategies such as FOC and DTC, particularly under simultaneous torque, flux, and secondary-plane current control requirements.

In this context, FCS-MPC has emerged as a versatile alternative for multiphase drive applications. One of its main advantages is the capability to directly determine the optimal switching state, eliminating the need for an external modulation stage. Nevertheless, in classical FCS-MPC implementations, applying a single voltage vector per sampling interval may increase harmonic distortion in the stator currents. To overcome this limitation, vector synthesis strategies have been proposed [24], [25], [26], among which the virtual-voltage-vector-based approach has gained significant attention due to its ease of implementation while maintaining the inherent simplicity of FCS-MPC.

The virtual voltage vector (VV) concept was initially introduced for five-phase IM drives as an effective means of mitigating secondary-plane currents [27]. The main principle underlying this approach is that two active voltage vectors are combined within a single sampling period to synthesise a VV that minimises the voltage components in the secondary-plane. As a result, improved current quality and reduced harmonic content can be achieved without significantly increasing the computational burden. Subsequently, this concept was extended to six-phase IM for both predictive current control (PCC) and PTC [28], [29]. In both cases, a significant reduction in secondary-plane $x-y$ currents was achieved, while preserving satisfactory control performance, ensuring accurate current tracking in PCC schemes and reliable torque tracking in PTC implementations.

Despite the significant progress achieved in predictive control of multiphase drives, simultaneously addressing weighting-factor elimination, effective secondary-plane current suppression, and computational efficiency remains a challenging problem. Existing predictive control strategies based on VV for secondary-plane current suppression typically rely on WF, whose empirical tuning is often cumbersome and dependent on the operating conditions, making the achievement of a suitable balance among the control objectives a non-trivial task. In contrast, existing weighting-factor-free PTC approaches do not explicitly address the minimisation of $x-y$ plane currents. Consequently, a PTC strategy capable of simultaneously achieving weighting-factor-free operation, effective secondary-plane current suppression, and reduced optimisation complexity has not yet been fully established in the literature.

To address this gap, this paper proposes a weighting-factor-free sequential model predictive torque control strategy with virtual voltage vector synthesis (SMPTC-VV) for six-phase IM drives. The proposed method combines a structured optimisation hierarchy with VV synthesis to achieve simultaneous regulation of electromagnetic torque, stator flux, and $x-y$ plane currents, while preserving the fast dynamic behaviour of classical PTC.

Building on preliminary work reported in [30] and [31], the current work introduces substantial methodological and structural enhancements, accompanied by comprehensive experimental validation under steady-state, dynamic, and parameter-mismatch conditions. The main contributions of the work are summarised as follows:

- Integration of virtual voltage vector synthesis into the previously reported [30] SMPTC formulation. Unlike the original strategy, which did not employ virtual vectors, the proposed approach explicitly mitigates non-torque-producing $x-y$ currents, achieving a 75.40% improvement in secondary-plane current suppression, and provides computational improvements of 75.66% and 50.66% relative to classical PTC and SMPTC, respectively.
- Reformulation of the sequential optimisation structure previously introduced in [31]. The original three-stage, three-cost-function structure is reduced to a two-stage configuration without performance degradation, simplifying the control process and enhancing computational efficiency. Additionally, delay compensation is incorporated to improve prediction accuracy and dynamic performance.
- Detailed analytical presentation of the duty-cycle selection employed in the virtual voltage vector synthesis process, explicitly showing the cancellation of $x-y$ plane voltage components.
- Development and analysis of a practical symmetrical PWM implementation framework for the proposed virtual voltage vectors, including virtual vectors classification and discussion of implementation-induced residual $x-y$ currents.

The remainder of this paper is organised as follows: Section II presents the mathematical model of the six-phase IM fed by a two-level converter. Section III explores the background of PTC. Section IV introduces the proposed SMPTC-VV strategy. Section V describes the experimental results. Finally, Section VI concludes the paper.

II. SYSTEM MATHEMATICAL MODEL

To develop the SMPTC strategy, the mathematical model of the six-phase IM drive system is needed. The drive consists of an asymmetrical six-phase IM fed by a two-level voltage source inverter (2L-VSI) connected to a DC-link voltage source (V_{dc}). The stator windings are arranged into two three-phase sets spatially shifted by 30° with isolated neutral points.

The inverter operation is described by a switching vector $\mathbf{S} = [S_a, S_d, S_b, S_e, S_c, S_f]$, where each binary variable $S_i \in \{0, 1\}$ represents the conduction state of the corresponding inverter leg. This configuration leads to a total of $2^6 = 64$ admissible switching states.

Based on the defined switching states, the stator phase voltage vectors $\boldsymbol{v}_s = [v_{sa}, v_{sd}, v_{sb}, v_{se}, v_{sc}, v_{sf}]^T$ can be obtained from the ideal 2L-VSI model as:

$$\boldsymbol{v}_s = \frac{V_{dc}}{3}\begin{bmatrix} 2 & 0 & -1 & 0 & -1 & 0 \\ 0 & 2 & 0 & -1 & 0 & -1 \\ -1 & 0 & 2 & 0 & -1 & 0 \\ 0 & -1 & 0 & 2 & 0 & -1 \\ -1 & 0 & -1 & 0 & 2 & 0 \\ 0 & -1 & 0 & -1 & 0 & 2 \end{bmatrix} \mathbf{S}^T \tag{1}$$

The model can be simplified by utilising vector space decomposition (VSD). This transformation employs a matrix denoted $\mathbf{T}$ to map the phase variables into three orthogonal planes: $\alpha-\beta$, $x-y$, and z_1-z_2. The electromagnetic torque and flux production are associated with the $\alpha-\beta$ plane, whereas the $x-y$ plane mainly contains harmonic components and is therefore related to additional losses. The third plane, z_1-z_2, corresponds to the zero-sequence components. Owing to the adopted two-neutral-point configuration, homopolar currents are inherently suppressed; consequently, the zero-sequence plane is excluded from the subsequent analysis.

Under these conditions and by adopting an invariant amplitude criterion, the stator voltage vector in the stationary reference frame $\boldsymbol{v}_{s_T} = [v_{s\alpha}, v_{s\beta}, v_{sx}, v_{sy}, v_{sz_1}, v_{sz_2}]^T$ is obtained as:

$$\boldsymbol{v}_{s_T} = \mathbf{T}\,\boldsymbol{v}_s$$

where $\mathbf{T}$ is defined as:

$$\mathbf{T} = \frac{1}{3}\begin{bmatrix} 1 & \frac{\sqrt{3}}{2} & -\frac{1}{2} & 0 & -\frac{1}{2} & -\frac{\sqrt{3}}{2} \\ 0 & \frac{1}{2} & -\frac{\sqrt{3}}{2} & -1 & \frac{\sqrt{3}}{2} & \frac{1}{2} \\ 1 & -\frac{\sqrt{3}}{2} & -\frac{1}{2} & 0 & -\frac{1}{2} & \frac{\sqrt{3}}{2} \\ 0 & \frac{1}{2} & \frac{\sqrt{3}}{2} & -1 & -\frac{\sqrt{3}}{2} & \frac{1}{2} \\ 1 & 0 & 1 & 0 & 1 & 0 \\ 0 & 1 & 0 & 1 & 0 & 1 \end{bmatrix} \tag{2}$$

The voltage vectors obtained after applying the VSD transformation can be represented in the $\alpha - \beta$ plane. The magnitude of each vector in this torque-producing plane is computed as:

$$|\mathbf{v}_{s_{T\alpha\beta}}| = \sqrt{v_{s\alpha}^2 + v_{s\beta}^2}. \tag{3}$$

For convenience, this quantity is normalised with respect to V_{dc}, i.e. $\frac{|\mathbf{v}_{s_{T\alpha\beta}}|}{V_{dc}}$. By evaluating it for all 64 switching states, it can be observed that the resulting vectors in the $\alpha - \beta$ plane naturally cluster into four groups according to their radial distance from the origin. These groups correspond to the voltage vector sets of the 2L-VSI and their corresponding normalised magnitudes are given by: $|V_l| = 0.6444\,V_{dc}$, $|V_{ml}| = 0.4714\,V_{dc}$, $|V_m| = 0.3333\,V_{dc}$, $|V_s| = 0.1736\,V_{dc}$, where V_l, V_{ml}, V_m, and V_s denote the large, medium-large, medium, and small voltage vectors, respectively. This classification arises purely from the geometric distribution of the 2L-VSI switching states after the VSD transformation for the asymmetrical six-phase topology with a 30° phase displacement.

A graphical representation of the 64 resulting voltage vectors in the stationary reference frame is shown in Fig. 1(a).

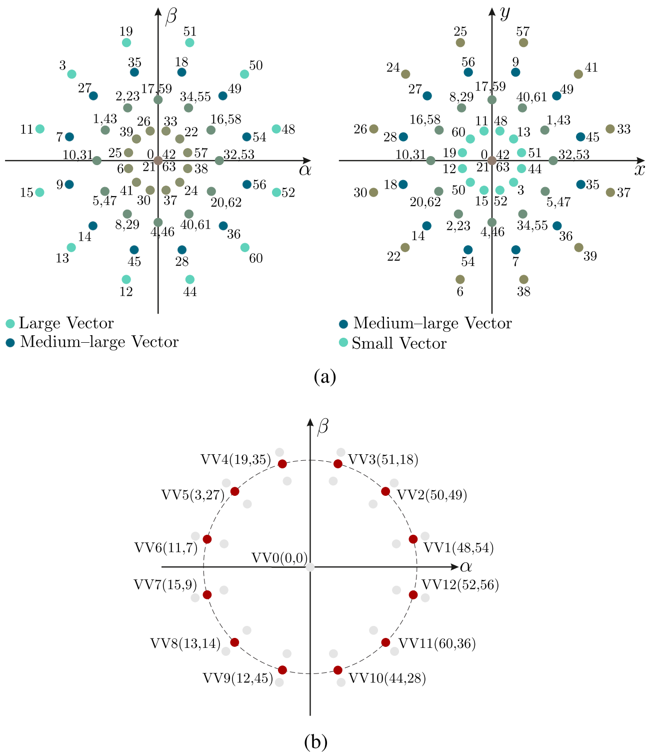

FIGURE 1. Voltage vector representation in the stationary reference frame obtained through VSD: (a) real voltage vectors mapped into the $\alpha - \beta$ and $x - y$ planes, and (b) virtual voltage vectors generated for the proposed control strategy.

III. PREDICTIVE TORQUE CONTROL

To enhance the performance and practical implementation of the proposed PTC scheme, two complementary techniques are incorporated: delay compensation and VV generation. Although these methods are well-established in the literature, their integration with the SMPTC strategy ensures accurate timing alignment between prediction and actuation and reduces $x - y$ plane currents.

A. DELAY COMPENSATION

To compensate for the intrinsic computational and actuation delays of the digital control platform, a two-step prediction horizon $(k+2)$ is adopted. In a digital implementation, the control action computed at sampling instant k cannot be applied instantaneously due to signal acquisition, computation, and switching update delays. Consequently, the selected switching state becomes effectively applied one sampling period later. By predicting the system states at $(k+2)$, the controller aligns the prediction model with the actual instant at which the control action takes effect, reducing the mismatch between predicted and actual system behaviour. This improves prediction accuracy and, consequently, enhances the dynamic performance of the predictive control scheme. Accordingly, the discrete-time state-space model is evaluated over the two-step prediction horizon $(k+2)$ as follows:

$$\boldsymbol{\psi}_{r[k+2]} = \mathbf{D}\boldsymbol{\psi}_{r[k+1]} + \mathbf{E}\boldsymbol{i}_{s[k+1]} \tag{4}$$

$$\boldsymbol{i}_{s[k+2]} = \mathbf{A}\boldsymbol{i}_{s[k+1]} + \mathbf{C}\boldsymbol{v}_{[k+1]} + \mathbf{B}\boldsymbol{\psi}_{r[k+1]} \tag{5}$$

$$\boldsymbol{\psi}_{s[k+2]} = \mathbf{F}\boldsymbol{i}_{s[k+2]} + \mathbf{G}\boldsymbol{\psi}_{r[k+2]} \tag{6}$$

$$\mathbf{T}_{e[k+2]} = 3P(\psi_{s\alpha[k+2]}i_{s\beta[k+2]} - \psi_{s\beta[k+2]}i_{s\alpha[k+2]}) \tag{7}$$

where $\boldsymbol{i}_{s[k]} = [i_{s\alpha[k]}, i_{s\beta[k]}, i_{sx[k]}, i_{sy[k]}]^T$ is the stator current vector, $\boldsymbol{\psi}_{r[k]} = [\psi_{r\alpha[k]}, \psi_{r\beta[k]}]^T$ is the rotor flux vector, $\boldsymbol{\psi}_{s[k]} = [\psi_{s\alpha[k]}, \psi_{s\beta[k]}, \psi_{sx[k]}, \psi_{sy[k]}]^T$ is the stator flux vector, and $\mathbf{T}_{e[k]}$ is the electromagnetic torque.

The matrices **A**–**G** depend on the electrical parameters of the machine and the sampling period, and are provided in the Appendix for completeness. The parameters include the stator and rotor resistances R_s and R_r, the stator and rotor inductances L_s and L_r, the mutual inductance M, the leakage inductance L_{ls}, the electrical rotor speed ω_r, and the number of pole pairs P.

B. VIRTUAL VECTORS

Although PTC ensures accurate tracking of the torque reference, the inherent voltage components in the $x-y$ plane can generate undesired current harmonics, thereby increasing copper losses in the machine. To mitigate these current harmonics present in the $x-y$ plane of the six-phase IM, a virtual-voltage-vector-based strategy is implemented. This technique is designed offline and generates a set of thirteen voltage vectors, as illustrated in Fig. 1(b), comprising the zero vector and a set of VVs.

Based on the voltage vector classification introduced in Section II, the VV are obtained by combining large (V_l) and medium–large (V_{ml}) vectors that share the same angular position in the $\alpha-\beta$ plane and exhibit opposite projections in the $x-y$ plane. Among the feasible vector pairs satisfying these conditions, the selected combinations correspond to those that maximise the resultant voltage magnitude in the $\alpha-\beta$ plane.

For the adopted VV construction, the normalised magnitudes of the vectors associated with V_l and V_{ml} are $0.1736V_{dc}$ and $0.4714V_{dc}$, respectively. These values correspond to the projections of the selected switching states onto the $x-y$ plane. Therefore, cancellation can be enforced by appropriately selecting their application times:

$$-0.1736V_{dc}d_l + 0.4714V_{dc}d_{ml} = 0 \tag{8}$$

where d_l and d_{ml} denote the duty cycles associated with the large and medium-large vectors, respectively. These duty cycles must also satisfy the sampling-period constraint:

$$d_l + d_{ml} = T_s \tag{9}$$

Solving (8) and (9) yields:

$$d_l = 0.73T_s, \qquad d_{ml} = 0.27T_s \tag{10}$$

Accordingly, the resulting VVi can be expressed as:

$$\mathrm{VVi} = d_l V_l + d_{ml} V_{ml} \tag{11}$$

Each VVi exhibits a magnitude approximately equal to 92.8% of the original V_l magnitude in the $\alpha-\beta$ plane, representing a favourable trade-off between voltage utilisation and harmonic mitigation.

IV. PROPOSED SEQUENTIAL MODEL PREDICTIVE CONTROL WITH VIRTUAL VECTORS

The following section presents a detailed description of the proposed SMPTC-VV strategy. The first subsection introduces the overall control scheme, the second subsection describes the algorithmic procedure, and the third subsection discusses the practical PWM implementation of the proposed VV.

A. SMPTC-VV SCHEME

The proposed control scheme is organised in a cascaded structure comprising an outer speed-control loop and an inner torque–flux control loop, as shown in Fig. 2. The measured stator currents and mechanical rotor speed ω_m are supplied to the corresponding loops for processing.

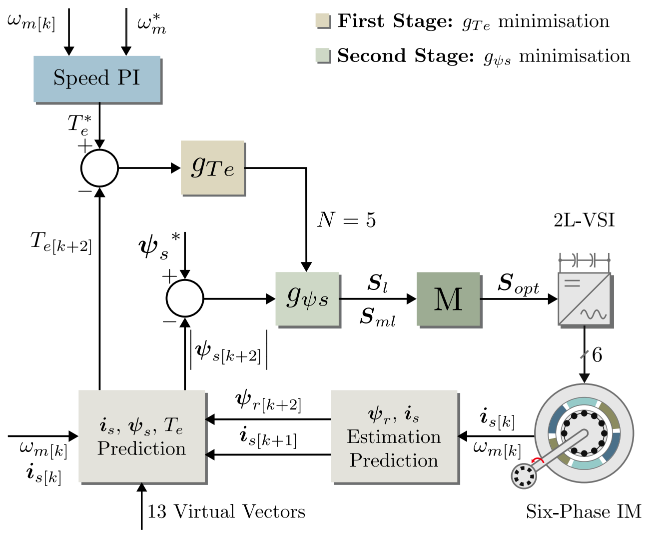

FIGURE 2. Block diagram of the proposed SMPTC-VV scheme. The diagram illustrates the cascaded speed and torque control loops, including flux and torque estimation, prediction models, cost function evaluation, and modulation for the 2L-VSI supplying the six-phase IM.

The primary purpose of the speed-control loop implemented using a PI controller is to generate the torque reference for the inner loop. The inner loop employs the proposed SMPTC-VV strategy, which operates sequentially to compute the optimal switching states for the two three-phase 2L-VSIs. This sequential execution ensures accurate regulation of the electromagnetic torque and flux. It provides fast dynamic response and effective decoupling between the mechanical and electrical subsystems.

To clarify the operation of the control scheme, the following subsection details the algorithmic sequence of the SMPTC-VV strategy.

B. SMPTC-VV ALGORITHM

The proposed SMPTC-VV scheme retains the fundamental structure of conventional predictive control, relying on system measurements and estimates. However, the cost function formulation is restructured to eliminate the need for WFs, thereby simplifying the optimisation process while preserving dynamic performance.

As illustrated in Fig. 3, the estimation of the rotor and stator fluxes is performed using the measured stator current and mechanical speed, together with the previously applied voltage vector. Subsequently, a unit horizon prediction of key variables—including stator current, stator flux, and rotor flux—is computed. The rotor flux is further refined in the second prediction horizon, leading to the evaluation of all 13 possible VV, from which the corresponding predicted stator currents, fluxes, and electromagnetic torques are obtained.

After all required predictions have been computed, the optimisation proceeds through a sequential hierarchical decision process rather than a simultaneous multi-objective evaluation. In the first stage, the torque-related cost function $g_{Te} = |T_e^* - T_{e[k+2]}|$ is evaluated for the 13 predicted torque values

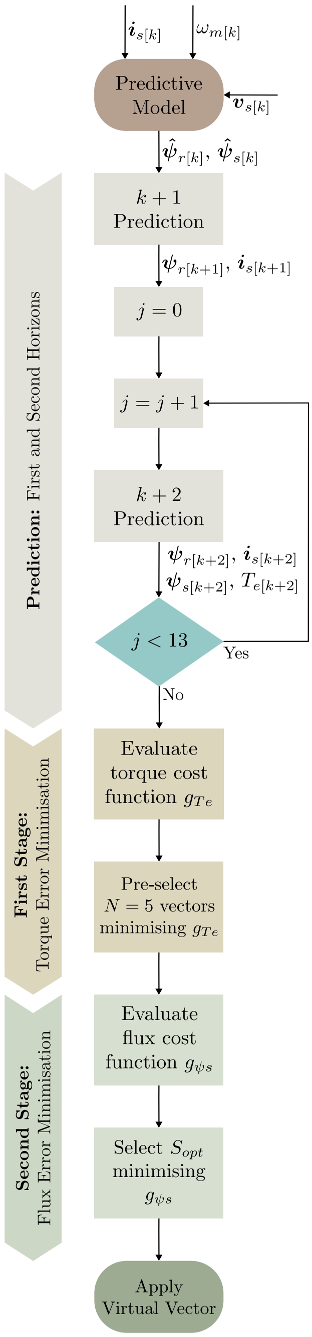

FIGURE 3. Flowchart of the proposed SMPTC-VV scheme illustrating the sequential evaluation of torque and flux cost functions for optimal VV selection.

associated with the candidate VV. The resulting costs are sorted in ascending order, enabling the preselection of the 5 VV that yield the lowest torque error. This reduced candidate set is then passed to the second stage, where the flux-related cost function $g_{\psi s} = \left||\psi_s^*| - |\psi_{s[k+2]}|\right|$ is analysed, and the VV that minimises the stator flux error is selected as the optimal switching state to be applied.

Subsequently, the 2L-VSI applies the switching state associated with the VV.

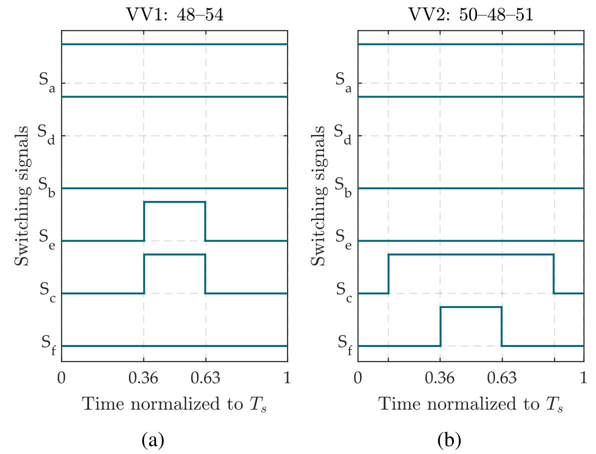

FIGURE 4. PWM pulse patterns used for virtual voltage vector synthesis in the proposed predictive control strategy: (a) switching pattern corresponding to VV1, and (b) switching pattern corresponding to VV2.

C. PRACTICAL PWM IMPLEMENTATION OF THE PROPOSED VIRTUAL VECTORS

Considering the practical implementation of the proposed VV using standard symmetrical PWM patterns, the VV can be classified into two groups, namely $\text{VV}_{\text{odd}} = \{\text{VV1}, \text{VV3}, \ldots, \text{VV11}\}$ and $\text{VV}_{\text{even}} = \{\text{VV2}, \text{VV4}, \ldots, \text{VV12}\}$.

The VV belonging to the VV_{odd} group can be synthesised directly using standard symmetrical PWM sequences due to the compatible arrangement of their switching states, as illustrated in Fig. 4(a). By contrast, the direct implementation of symmetrical PWM patterns for the VV_{even} group is not always feasible because of duty cycle conflicts between the involved switching states, as depicted in Fig. 4(b).

For clarity, the implementation of VV1 and VV2 is discussed as representative examples. The virtual vector VV1 is synthesised using the large vector $V_{l|48|}$ and the medium-large vector $V_{ml|54|}$, applied with duty cycles of 0.73 and 0.27, respectively. Since both switching states can be naturally arranged within a symmetrical PWM sequence, the implementation can be achieved directly.

Conversely, VV2 should ideally be synthesised using the large vector $V_{l|50|}$ and the medium-large vector $V_{ml|49|}$. However, due to the PWM constraints associated with the VV_{even} group, the medium-large vector cannot be generated directly within a standard symmetrical PWM pattern. Therefore, an equivalent switching sequence is employed, where $V_{ml|49|}$ is replaced by the combination of the large vectors $V_{l|48|}$ and $V_{l|51|}$, as shown in Fig. 5.

As a consequence, a slight deviation in the resulting VV magnitude is introduced. For the analysed case, the obtained VV magnitude becomes equal to that of a large vector. This practical limitation inevitably produces a small residual current in the secondary $x-y$ subspace. Nevertheless, this effect remains limited and is inherent to the real-time PWM implementation of the proposed VV synthesis rather than to an incorrect application of the method.

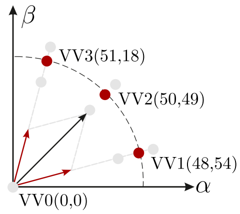

FIGURE 5. Representative VV in the $\alpha - \beta$ plane, illustrating the practical implementation of VV_{even} vector, where the medium-large vector $V_{ml|49|}$ is equivalently synthesised using the large vectors $V_{l|48|}$ and $V_{l|51|}$.

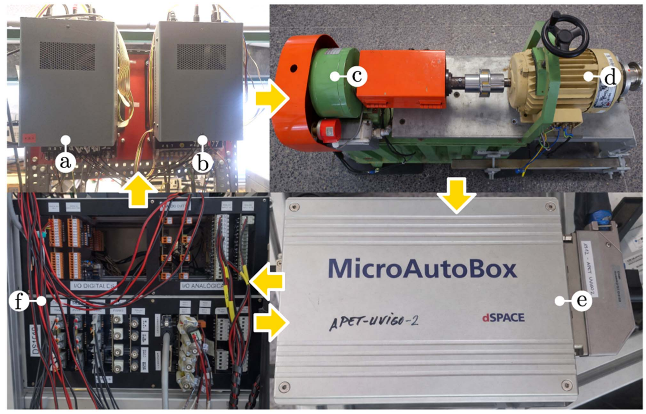

FIGURE 6. Experimental test bench: (a) three-phase 2L-VSI, (b) three-phase 2L-VSI, (c) mechanical load, (d) six-phase IM, (e) dSpace control unit, (f) expansion boxes.

TABLE 1. Electrical and Mechanical Parameters of the Six-Phase IM

Parameter	Value	Parameter	Value
R_r (Ω)	6.9	R_s (Ω)	6.7
L_s (mH)	654.4	L_r (mH)	626.8
L_m (mH)	614	L_{ls} (mH)	5.3
$\omega_{m,\text{rated}}$ (r/min)	2540	P_w (kW)	1.5
J_i (kg·m^2)	0.07	B_i (kg·m^2/s)	0.0004
P	1	$T_{e,\text{rated}}$ (N·m)	5.6
V_s (V)	220	f_{rated} (Hz)	50
$i_{s,\text{rms}}$ (A)	2.2	V_{dc} (V)	400
Efficiency (%)	86	Power factor	0.8

V. EXPERIMENTAL VALIDATION

A. TEST BENCH

The proposed algorithms were experimentally validated on a laboratory test bench comprising a six-phase IM supplied by two conventional three-phase 2L-VSIs and a regulated DC source. The power converter consists of two conventional three-phase 2L-VSIs implemented using Semikron SK-30GB-123 modules, with each leg controlled by a Semikron SKHI 20opA driver. All six IGBT legs are supplied from a common DC bus. The control algorithms were implemented on a dSPACE MicroAutoBox II (MABX II) real-time rapid-prototyping platform, using MATLAB/Simulink. The parameters of the six-phase IM were obtained from standstill tests and standard AC time-domain identification techniques; these values are listed in Table 1.

Phase currents were measured using LA 55-P Hall-effect sensors configured with multi-turn windings to enhance accuracy at low current levels. The sensors provide a bandwidth from DC to 200 kHz, and their analogue outputs were digitised via a 16-bit A/D converter. The mechanical position was acquired from a 1024-ppr incremental encoder, from which rotor speed was computed. The encoder signals are processed by the FPGA embedded in the dSPACE platform and updated at each sampling period for use in the control loop, which is sequentially executed by the processor. A variable mechanical load was applied using a 5-hp eddy-current brake with the applied braking torque manually regulated by adjusting its supply current. The complete experimental arrangement is shown in Fig. 6.

B. FIGURES OF MERIT

To provide a quantitative basis for performance assessment, key figures of merit were defined. The root mean square error (RMSE) was calculated for the electromagnetic torque, the stator flux, and the currents in the $x - y$ plane. The torque RMSE reflects the accuracy of torque tracking, while RMSE_{xy} quantifies the amplitude of the secondary-plane currents, indicating the effectiveness of current decoupling achieved by the control algorithm. The RMSE is defined as:

$$\text{RMSE}_m = \sqrt{\frac{1}{N}\sum_{k=1}^{N}\left(m_{[k]} - m^*_{[k]}\right)^2}$$

where N represents the number of samples, $m^*_{[k]}$ denotes the reference variable, $m_{[k]}$ the measured variable, and $m \in \{T_e, \psi_s, x, y\}$. RMSE_{xy} is computed as the average of RMSE_x and RMSE_y.

In addition, the total harmonic distortion (THD) of the stator current was evaluated along the α-axis and a-phase to assess waveform quality and harmonic content. The THD is defined as:

$$\text{THD} = \sqrt{\frac{1}{i_{s1}^2}\sum_{j=2}^{N}(i_{sj})^2}$$

where i_{s1} denotes the fundamental component of the stator current, and i_{sj} represents the jth harmonic component.

Furthermore, an additional metric considered here is the percentage improvement, defined as

$$(\%)\text{Imp}_V = 100 \times \frac{U - V}{U}$$

where V and U denote the evaluated figure of merit obtained with the proposed SMPTC-VV strategy and with the reference control strategy, respectively. The considered figures of merit include the THD, the RMSE of torque, stator flux, and $x - y$ current tracking, as well as the computational burden quantified in terms of floating-point operations (FPOs) per sampling period.

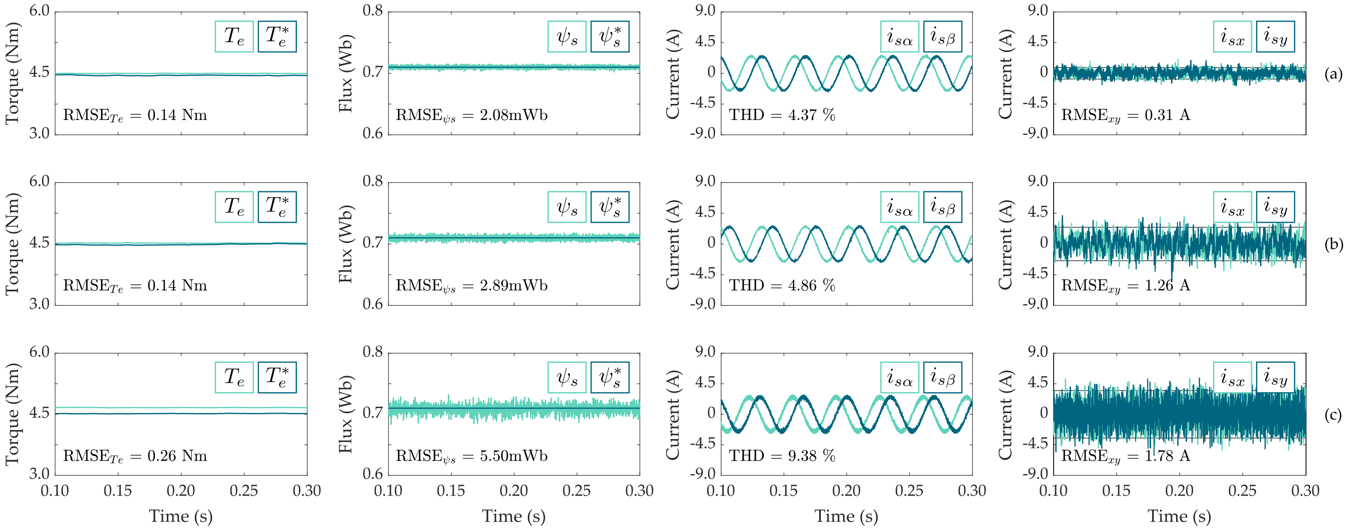

FIGURE 7. **Steady-state experimental waveforms of the Six-Phase IM under the (a) proposed SMPTC-VV, (b) SMPTC, and (c) classical PTC control schemes. From left to right: electromagnetic torque and reference, stator flux magnitude and reference, $\alpha - \beta$ stator current components, and $x - y$ stator current components. Each subplot includes the corresponding quantitative performance indices (THD or RMSE) for comparison. The proposed SMPTC-VV achieves improved flux regulation and more effective suppression of $x - y$ currents compared with conventional approaches.**

TABLE 2. **Control Parameters of the Evaluated Strategies**

Parameter	Proposed SMPTC-VV	SMPTC	Classical PTC
Control structure	2 stages	3 stages	single-stage
Cost function	g_{Te}, $g_{\psi s}$	g_{xy} g_{Te}, $g_{\psi s}$	$g_{Te} + 10\, g_{\psi_s} + 0.2\, g_{xy}$
Weighting factors	Not required	Not required	Required
Number of evaluated vectors	13	64	64
Selected candidates	$N = 5$	$N_1 = 13$ $N_2 = 4$	All
Average switching frequency (kHz)	10.20	5.79	2.93

C. CONTROL IMPLEMENTATION AND PARAMETERISATION

The control-related parameters used in the experimental validation are summarised in Table 2. The outer-loop speed controller employs a PI regulator tuned with a damping ratio of $\zeta = 0.61$ and a design factor $\alpha_s = 1.5$, with these values consistently applied across all evaluated strategies.

The inner loop is based on predictive control. The proposed SMPTC-VV adopts a sequential multi-stage cost function, as described in Section IV, where torque and stator flux errors are evaluated independently, eliminating the need for WF. The SMPTC strategy follows a similar multi-stage structure, including an additional stage to minimise the current components in the $x - y$ subspace, whereas the classical PTC employs a single-stage cost function that combines torque and stator-flux errors via WF.

A common sampling frequency of 22 kHz was used for all strategies, establishing equivalent control-bandwidth conditions while allowing the switching frequency to vary across algorithms. This enables the assessment of intrinsic algorithmic performance, with switching behaviour treated separately in the subsequent analysis.

D. PERFORMANCE AND COMPUTATIONAL EFFORT COMPARISON OF PTC, SMPTC AND SMPTC-VV

The steady-state performance of the six-phase IM under the proposed SMPTC-VV control was first evaluated to verify the accurate regulation of torque and flux. Fig. 7 illustrates the measured waveforms of electromagnetic torque, stator flux magnitude and stator currents in $\alpha - \beta$ and $x - y$ planes during steady-state operation at 1500 r/min speed and 80% of nominal load conditions (T_L). The results shown in Fig. 7(a) demonstrate that the proposed control strategy effectively minimises the secondary-plane currents, together with reduced torque ripple and flux tracking error.

The SMPTC-VV controller yielded a THD_α of 4.37% for the α-axis current, a THD_a of 26.76 % for the a-phase stator current, an RMSE_{Te} of 0.14 Nm for torque tracking, and an RMSE_{xy} of 0.31 A, indicating low harmonic distortion, accurate torque regulation, and effective suppression of non-torque-producing currents.

To further evaluate the proposed SMPTC-VV strategy, experimental comparisons with conventional SMPTC and classical PTC were carried out under identical steady-state operating conditions. The corresponding waveforms are presented in Fig. 7(b) and (c), respectively, whereas the full set of figures of merit is summarised in Table 3. The results indicate that the proposed SMPTC-VV attains a torque tracking accuracy comparable to that of SMPTC, while achieving a 46.15% improvement over classical PTC. In addition, improvements of 28.03% and 31.13% are obtained in flux regulation with respect to SMPTC and classical PTC, respectively.

TABLE 3. **Steady-State Performance Analysis of Proposed SMPTC-VV, SMPTC and Classical PTC**

Method	$RMSE_{Te}$ (N.m)	$RMSE_{\psi s}$ (mWb)	$RMSE_{xy}$ (A)	THD_{α} (%)	THD_{a} (%)
Proposed SMPTC-VV	0.14	2.08	0.31	4.37	26.76
SMPTC	0.14	2.89	1.26	4.86	58.51
Classical PTC	0.26	5.50	1.78	9.38	86.90

TABLE 4. **Steady-State Performance Analysis of Proposed SMPTC-VV, SMPTC and Classical PTC At the Same Average Switching Frequency**

Method	$RMSE_{Te}$ (N.m)	$RMSE_{\psi s}$ (mWb)	$RMSE_{xy}$ (A)	THD_{α} (%)	THD_{a} (%)
Proposed SMPTC-VV	0.94	5.96	0.19	9.87	13.32
SMPTC	0.23	6.30	1.50	5.54	68.79
Classical PTC	0.26	5.50	1.78	9.38	86.90

TABLE 5. **Dynamic Performance Under Speed Reversal Conditions**

Method	$RMSE_{Te}$ (N.m)	$RMSE_{\psi s}$ (mWb)	$RMSE_{xy}$ (A)
Proposed SMPTC-VV	0.13	2.19	0.43
SMPTC	0.14	3.13	1.24
Classical PTC	0.33	5.64	1.37

The $\alpha-\beta$ stator current waveforms remain sinusoidal across all cases; nevertheless, the proposed control strategy achieves improvements of 10.08% and 53.41% in THD_{α}, and 54.26% and 69.21% in THD_{a}, with respect to SMPTC and classical PTC, respectively. Moreover, the $x-y$ current components are markedly mitigated under the proposed control, with improvements of 75.40% and 82.58% relative to SMPTC and classical PTC, respectively. This reduction in non-torque-producing currents enhances overall current quality and supports the adoption of the SMPTC-VV strategy over conventional predictive control schemes.

To complement the performance comparison, the computational effort was examined. A detailed analysis shows that, for each sampling period, the proposed $(k+2)$ SMPTC-VV algorithm performs 88 FPOs in the first horizon, including estimation and prediction of rotor flux and stator current. The second horizon, which considers the prediction of stator currents, rotor flux, stator flux, and electromagnetic torque over 13 candidate voltage vectors, requires 728 FPOs. The evaluation of the torque and flux cost functions adds 104 FPOs. Subsequently, the sorting and selection of the optimal voltage vector—first ordering by minimising the torque cost function and then the flux cost function over the top $N=5$ candidates—requires 42 FPOs. Finally, assigning the selected switch states adds 4 FPOs. Overall, this results in 966 FPOs per sampling period, reflecting the computational effort required by the algorithm for the two-step prediction, cost function evaluation, and optimal vector selection.

In contrast, the classical PTC implementation, which evaluates all 64 voltage vectors within a single-stage cost function, requires 3968 FPOs per sampling period. Likewise, the SMPTC implementation based on external voltage vectors requires 1958 FPOs per sampling period [30]. Accordingly, the proposed SMPTC-VV achieves computational improvements of 75.66% and 50.66% compared to classical PTC and SMPTC, respectively, providing a consistent reference for assessing the computational demand of the proposed strategy.

E. PERFORMANCE EVALUATION AT THE SAME SWITCHING FREQUENCY

To further assess the proposed strategy, an additional comparison was performed at an average switching frequency of 3 kHz. Since the proposed SMPTC-VV inherently operates at a higher switching frequency than SMPTC and classical PTC, its sampling frequency was reduced accordingly. The corresponding steady-state performance is summarised in Table 4.

The results show that the proposed SMPTC-VV strategy continues to effectively suppress the currents in the $x-y$ plane, outperforming both SMPTC and classical PTC. However, torque tracking performance deteriorates due to the reduced sampling frequency required to achieve the same average switching frequency, rather than the VV concept itself.

The increased sampling interval reduces prediction accuracy, delay-compensation effectiveness, and control bandwidth, partially compromising the fast dynamic response of PTC while preserving the capability of the proposed strategy to suppress $x-y$ plane currents.

F. DYNAMIC RESPONSE

The transient behaviour of the proposed SMPTC-VV control scheme was experimentally evaluated to verify its dynamic performance under abrupt changes in operating conditions.

For the speed reversal test, the reference speed was abruptly varied from +1000 r/min to −1000 r/min, while maintaining a load torque equal to 80% of the nominal value. The corresponding experimental results are presented in Fig. 8 and Table 5. Following the speed reversal, the rotor speed tracks the new reference and stabilises without steady-state error, while the $\alpha-\beta$ stator current components recover their sinusoidal waveform after a short transient. The settling times are 4.51 s, 4.30 s, and 4.50 s for SMPTC-VV, SMPTC, and classical PTC, respectively, according to the 5% criterion.

The proposed SMPTC-VV achieves torque tracking accuracy improvements of 7.14% and 60.61% with respect to SMPTC and classical PTC, respectively. Stator flux regulation is also improved by 30.03% and 61.17%. In addition, a marked reduction in the $x-y$ current components is observed, with improvements of 65.32% and 68.61% compared to SMPTC and classical PTC, respectively.

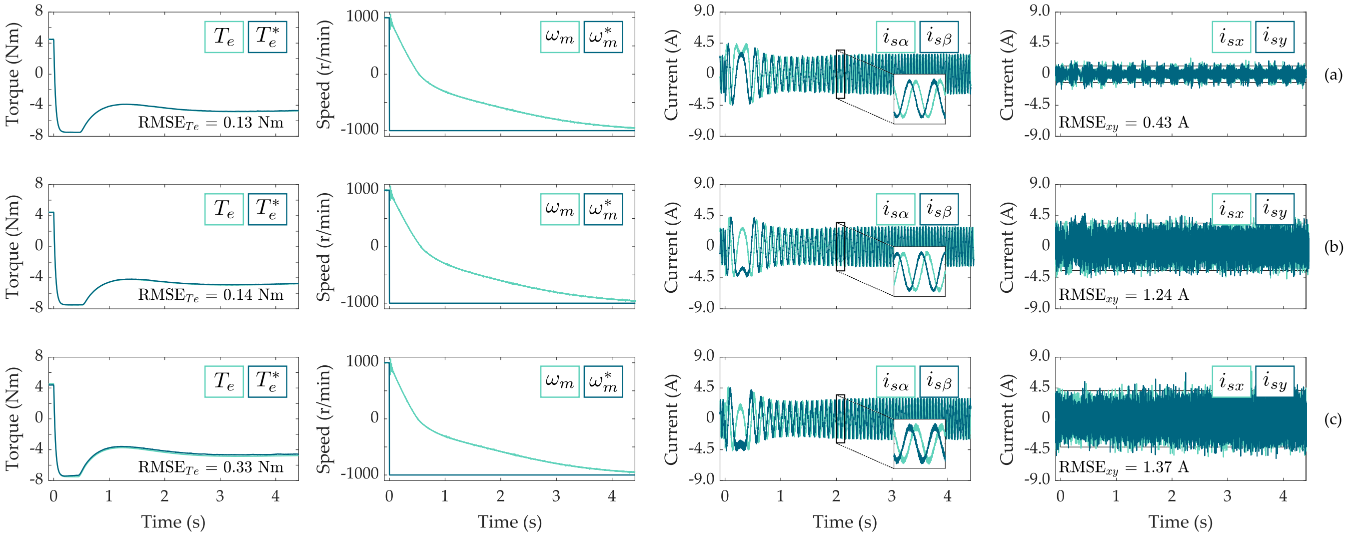

FIGURE 8. Experimental results of the speed reversal test for (a) proposed SMPTC-VV, (b) SMPTC, and (c) classical PTC control schemes. For each control strategy, from left to right: electromagnetic torque, rotor mechanical speed, $\alpha - \beta$ stator current components, and $x - y$ stator current components. The test involves a reference speed reversal from +1000 r/min to −1000 r/min at 80% of the nominal load torque. The results enable a direct comparison of torque tracking performance, dynamic response, and $x - y$ current suppression among the evaluated methods.

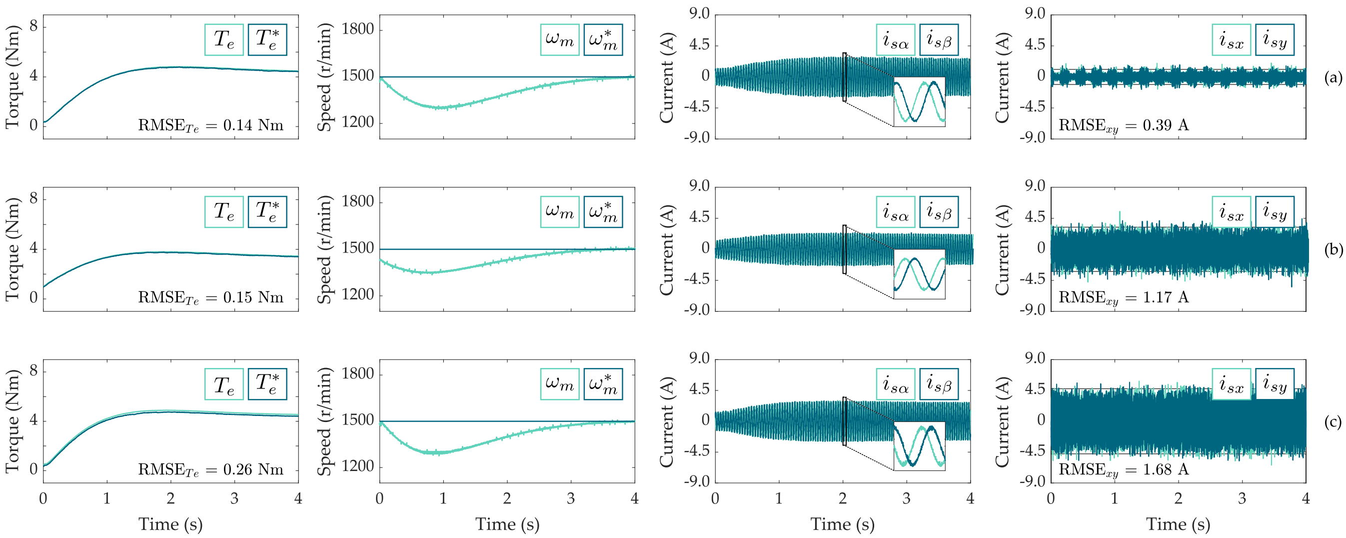

FIGURE 9. Experimental results of the torque step response for (a) proposed SMPTC-VV, (b) SMPTC, and (c) classical PTC control schemes. For each control strategy, from left to right: electromagnetic torque, rotor mechanical speed, $\alpha - \beta$ stator current components, and $x - y$ stator current components. The test involves a sudden increase in load torque from 0 to 80% of the nominal value at a constant reference speed of 1500 r/min. The results enable a direct comparison of torque tracking performance, dynamic response, and $x - y$ current suppression among the evaluated methods.

For the load torque step test, the load torque is abruptly changed from 0 to 80% of its nominal value while maintaining the speed reference at 1500 r/min, as shown in Fig. 9 and Table 6. Following the load torque step, the rotor speed briefly decreases before rapidly returning to the reference value, while the $\alpha - \beta$ stator current components promptly reach their new steady-state amplitudes after a short transient.

The proposed SMPTC-VV strategy achieves accurate torque tracking, with improvements of 6.67% and 46.15%

TABLE 6. Dynamic Performance Under Torque Step Conditions

Method	RMSE$_{Te}$ (N.m)	RMSE$_{\psi_s}$ (mWb)	RMSE$_{xy}$ (A)
Proposed SMPTC-VV	0.14	2.12	0.39
SMPTC	0.15	3.13	1.17
Classical PTC	0.26	5.41	1.68

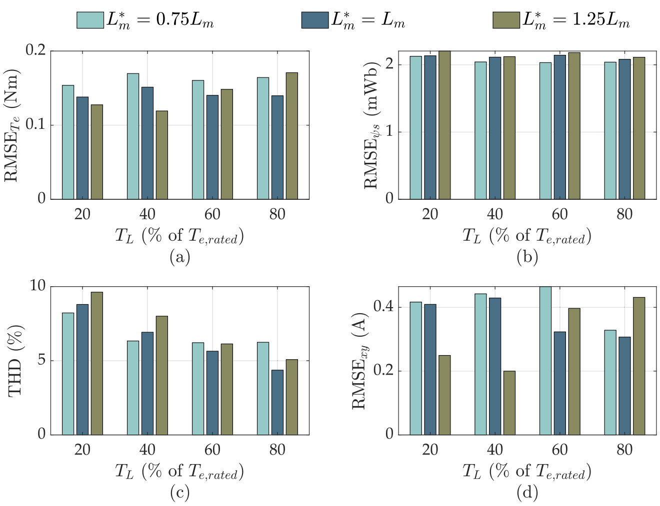

FIGURE 10. Sensitivity analysis under magnetising inductance mismatch (±25% L_m): (a) torque tracking performance (RMSE_{Te}), (b) stator flux tracking performance ($\mathrm{RMSE}_{\psi s}$), (c) α current harmonic distortion (THD), (d) $x-y$ current suppression (RMSE).

over SMPTC and classical PTC, respectively. Stator flux regulation is also improved by 32.27% and 60.81%. In addition, the $x-y$ current components are significantly reduced, yielding improvements of 66.67% and 76.79% compared to SMPTC and classical PTC, respectively.

These results confirm that the proposed SMPTC-VV controller maintains excellent dynamic performance during torque transients. The scheme achieves rapid torque and speed recovery, with minimal coupling effects between planes. Most notably, the $x-y$ current components remain effectively suppressed even under dynamic load variations, consistent with the steady-state findings and reinforcing the superior current quality achieved by the proposed control strategy. Furthermore, the consistent performance observed across both speed reversal and load torque step tests highlights the robustness of the proposed strategy under different transient operating conditions.

G. CONTROL SENSITIVITY TO PARAMETER MISMATCH

Parameter variations are inevitable during continuous machine operation due to thermal effects, ageing, and magnetic saturation. This subsection evaluates the robustness of the proposed SMPTC-VV control scheme under parameter mismatch conditions. In particular, a ±25% variation of the magnetising inductance L_m is intentionally introduced in the control algorithm, as this parameter is known to be highly sensitive to magnetic saturation and operating point variations in IM.

To assess the impact of parameter mismatch, the rotor speed was maintained at 1500 r/min for all test cases, while L_m^* was varied to $0.75L_m$, L_m, and $1.25L_m$. For each L_m^* setting, four load torque levels corresponding to 20%, 40%, 60%, and 80% of the nominal torque were evaluated. The resulting figures of merit, including RMSE_{T_e}, $\mathrm{RMSE}_{\psi s}$, current THD, and RMSE_{xy}, are summarised in Fig. 10. Note that L_m^* denotes the magnetising inductance value used in the control algorithm, while L_m corresponds to the actual machine parameter.

It can be observed that the proposed SMPTC-VV scheme maintains stable performance across the entire range of L_m variations and load conditions. Although minor variations in the evaluated figures of merit are observed as L_m deviates from its nominal value, all performance indices remain within acceptable limits. In particular, the $x-y$ current components remain effectively suppressed, confirming the robustness of the proposed control strategy against magnetising inductance mismatch.

Overall, the experimental results obtained from steady-state operation, dynamic tests, and parameter sensitivity analysis demonstrate the effectiveness of the proposed SMPTC-VV control scheme. Accurate torque and flux regulation are achieved, along with a fast transient response and strong robustness against magnetising inductance mismatch. These results confirm the practical viability of the proposed approach and motivate the conclusions presented in the following section.

VI. CONCLUSION

This paper has presented a weighting-factor-free sequential model predictive torque control strategy with virtual voltage vector synthesis (SMPTC-VV) for a six-phase induction machine supplied by dual two-level voltage source inverters. The proposed control scheme restructures the conventional predictive torque control formulation through a sequential cost-function evaluation, eliminating the need for heuristic weighting-factor tuning while preserving the fast dynamic characteristics of predictive torque control. In addition, the integration of virtual voltage vectors enables effective suppression of harmonic components in the $x-y$ plane.

The proposed approach has been experimentally validated under steady-state operation, dynamic speed and load transients, and magnetising inductance mismatch conditions. The results demonstrate accurate torque and flux regulation, improved current quality, and effective suppression of non-torque-producing $x-y$ currents. In particular, the proposed strategy achieves up to 75.40% and 82.58% improvements in secondary-plane current suppression compared with SMPTC and classical PTC, respectively.

Furthermore, computational analysis reveals substantial reduction in floating-point operations, with improvements of 75.66% and 50.66% relative to classical PTC and SMPTC, respectively, ensuring real-time feasibility while enhancing computational efficiency.

Overall, the proposed SMPTC-VV strategy provides a computationally efficient and experimentally validated predictive torque control solution for multiphase induction machines, simultaneously enhancing current quality, explicitly mitigating secondary-plane currents, and maintaining robust performance across a wide range of operating conditions.

APPENDIX

$$\mathbf{A}=\begin{bmatrix} a_{11} & 0 & 0 & 0\\ 0 & a_{22} & 0 & 0\\ 0 & 0 & a_{33} & 0\\ 0 & 0 & 0 & a_{44}\end{bmatrix};\ \mathbf{B}=\begin{bmatrix} \frac{R_r M_m T_s}{\sigma L_s L_r^2} & \frac{\omega_r M_m T_s}{\sigma L_s L_r}\\ -\frac{\omega_r M_m T_s}{\sigma L_s L_r} & \frac{R_r M_m T_s}{\sigma L_s L_r^2}\\ 0 & 0\\ 0 & 0\end{bmatrix};$$

$$\text{Being}\quad a_{11}=a_{22}=1-\frac{T_s}{\sigma\tau_s}-\frac{(1-\sigma)T_s}{\sigma\tau_r};$$

$$a_{33}=a_{44}=1-\frac{R_s T_s}{L_{ls}};$$

$$\mathbf{C}=\begin{bmatrix} \frac{T_s}{\sigma L_s} & 0 & 0 & 0\\ 0 & \frac{T_s}{\sigma L_s} & 0 & 0\\ 0 & 0 & \frac{T_s}{\sigma L_s} & 0\\ 0 & 0 & 0 & \frac{T_s}{\sigma L_s}\end{bmatrix};$$

$$\mathbf{D}=\begin{bmatrix} 1-\frac{T_s}{\tau_r} & -\omega_r T_s\\ \omega_r T_s & 1-\frac{T_s}{\tau_r}\end{bmatrix};\ \mathbf{E}=\begin{bmatrix} \frac{M_m T_s}{\tau_r} & 0 & 0 & 0\\ 0 & \frac{M_m T_s}{\tau_r} & 0 & 0\end{bmatrix};$$

$$\mathbf{F}=\begin{bmatrix} \sigma L_s & 0 & 0 & 0\\ 0 & \sigma L_s & 0 & 0\\ 0 & 0 & L_{ls} & 0\\ 0 & 0 & 0 & L_{ls}\end{bmatrix};\ \mathbf{G}=\begin{bmatrix} \frac{M_m}{L_r} & 0\\ 0 & \frac{M_m}{L_r}\\ 0 & 0\\ 0 & 0\end{bmatrix};$$

$$\text{Being}\quad \sigma=1-M_m^2/L_sL_r;\ \tau_s=L_s/R_s;\ \tau_r=L_r/R_r;$$

$$M_m=3L_m.$$

REFERENCES

[1] F. Wang, Z. Zhang, X. Mei, J. Rodrıǵuez, and R. Kennel, "Advanced control strategies of induction machine: Field oriented control, direct torque control and model predictive control," *Energies*, vol. 11, no. 1, 2018, Art. no. 120.

[2] D. Song et al., "ANN-based model predictive control for hybrid energy storage systems in DC microgrid," *Protection Control Modern Power Syst.*, vol. 10, no. 4, pp. 1–15, Jul. 2025.

[3] J. Hu and K. W. E. Cheng, "Predictive control of power electronics converters in renewable energy systems," *Energies*, vol. 10, no. 4, 2017, Art. no. 515.

[4] X. Wu, C. Xue, and Y. Li, "Multirate FCS-MPC for parallel dual-converter-fed PMSM drives with reduced circulating currents," *IEEE J. Emerg. Sel. Topics. Power Electron.*, vol. 13, no. 2, pp. 1638–1649, Apr. 2025.

[5] J. Rodriguez et al., "Latest advances of model predictive control in electrical drives—Part II: Applications and benchmarking with classical control methods," *IEEE Trans. Power Electron.*, vol. 37, no. 5, pp. 5047–5061, May 2022.

[6] J. Rodriguez et al., "Latest advances of model predictive control in electrical drives—Part I: Basic concepts and advanced strategies," *IEEE Trans. Power Electron.*, vol. 37, no. 4, pp. 3927–3942, Apr. 2022.

[7] S. A. Davari, V. Nekoukar, S. Azadi, F. Flores-Bahamonde, C. Garcia, and J. Rodriguez, "Discrete optimization of weighting factor in model predictive control of induction motor," *IEEE Open J. Ind. Electron. Soc.*, vol. 4, pp. 573–582, 2023.

[8] M. Novak, H. Xie, T. Dragicevic, F. Wang, J. Rodriguez, and F. Blaabjerg, "Optimal cost function parameter design in predictive torque control (PTC) using artificial neural networks (ANN)," *IEEE Trans. Ind. Electron.*, vol. 68, no. 8, pp. 7309–7319, Aug. 2021.

[9] S. Xu, C. Yao, G. Ren, Z. Sun, S. Wu, and G. Ma, "Weighting factors autotuning of FCS-MPC for hybrid ANPC inverter in PMSM drives based on deep residual networks," *IEEE Trans. Ind. Electron.*, vol. 39, no. 12, pp. 16540–16552, Dec. 2024.

[10] H. Fretes et al., "Pareto optimal weighting factor design of predictive current controller of a six-phase induction machine based on particle swarm optimization algorithm," *IEEE J. Emerg. Sel. Topics Power Electron.*, vol. 10, no. 1, pp. 207–219, Feb. 2022.

[11] E. Zerdali, M. Rivera, and P. Wheeler, "A review on weighting factor design of finite control set model predictive control strategies for AC electric drives," *IEEE Trans. Power Electron.*, vol. 39, no. 8, pp. 9967–9981, Aug. 2024.

[12] R. Fu, "Robust model predictive flux control of PMSM drive using a compensated stator flux predictor," *IEEE Access*, vol. 9, pp. 136736–136743, 2021.

[13] C. Xia, T. Liu, T. Shi, and Z. Song, "A simplified finite-control-set model-predictive control for power converters," *IEEE Trans. Ind. Informat.*, vol. 10, no. 2, pp. 991–1002, May 2014.

[14] E. Zerdali, M. Rivera, P. Zanchetta, P. Wheeler, and L. Ristić, "Encoderless predictive speed and torque control of an induction motor," in *Proc. 22nd Int. Symp. Power Electron.*, 2023, vol. 1, pp. 1–6.

[15] M. Norambuena, J. Rodriguez, Z. Zhang, F. Wang, C. Garcia, and R. Kennel, "A very simple strategy for high-quality performance of AC machines using model predictive control," *IEEE Trans. Power Electron.*, vol. 34, no. 1, pp. 794–800, Jan. 2019.

[16] M. A. Frikha, J. Croonen, K. Deepak, Y. Benômar, M. El Baghdadi, and O. Hegazy, "Multiphase motors and drive systems for electric vehicle powertrains: State of the art analysis and future trends," *Energies*, vol. 16, no. 2, 2023, Art. no. 768.

[17] M. Bermúdez, F. Barrero, C. Martıń, and M. Perales, "Performance analysis of direct torque controllers in five-phase electrical drives," *Appl. Sci. (Basel)*, vol. 11, no. 24, 2021, Art. no. 11964.

[18] F. Barrero and M. J. Duran, "Recent advances in the design, modeling, and control of multiphase machines—Part I," *IEEE Trans. Ind. Electron.*, vol. 63, no. 1, pp. 449–458, Jan. 2016.

[19] A. G. Yepes, I. Gonzalez-Prieto, O. Lopez, M. J. Duran, and J. Doval-Gandoy, "A comprehensive survey on fault tolerance in multiphase AC drives, Part 2: Phase and switch open-circuit faults," *Machines (Basel)*, vol. 10, no. 3, 2022, Art. no. 221.

[20] M. A. Abu-Seif et al., "Data-driven-based vector space decomposition modeling of multiphase induction machines," *IEEE Trans. Energy Convers.*, vol. 38, no. 3, pp. 2061–2074, Sep. 2023.

[21] H. Toliyat and H. Xu, "A novel direct torque control (DTC) method for five-phase induction machines," in *Proc. APEC 2000. 15th Annu. IEEE Appl. Power Electron. Conf. Expo.*, 2000, vol. 1, pp. 162–168.

[22] R. I. Bojoi, F. Farina, F. Profumo, and A. Tenconi, "Dual-three phase induction machine drives control—A survey," *IEEJ Trans. Ind. Appl.*, vol. 126, pp. 420–429, 2006.

[23] Z. Liu, Y. Li, and Z. Zheng, "A review of drive techniques for multiphase machines," *CES Trans. Elect. Machines Syst.*, vol. 2, no. 2, pp. 243–251, 2018.

[24] P. Gonçalves, S. Cruz, and A. Mendes, "Finite control set model predictive control of six-phase asymmetrical machines—An overview," *Energies*, vol. 12, no. 24, 2019, Art. no. 4693.

[25] M. R. Arahal, M. G. Satué, F. Barrero, and J. Martıńez-Heredia, "Model reference adaptive predictive current control of six-phase induction machine," *IEEE Trans. Ind. Electron.*, vol. 72, no. 11, pp. 10927–10934, Nov. 2025.

[26] A. González-Prieto, I. González-Prieto, M. J. Duran, J. J. Aciego, and P. Salas-Biedma, "Current harmonic mitigation using a multi-vector solution for MPC in six-phase electric drives," *IEEE Access*, vol. 9, pp. 117761–117771, 2021.

[27] L. Zheng, J. E. Fletcher, B. W. Williams, and X. He, “A novel direct torque control scheme for a sensorless five-phase induction motor drive,” *IEEE Trans. Ind. Electron.*, vol. 58, no. 2, pp. 503–513, Feb. 2011.
[28] O. Gonzalez et al., “Virtual-vector-based predictive torque control for six-phase IM with reduced computational burden and copper losses,” *IEEE Open J. Power Electron.*, vol. 6, pp. 1371–1381, 2025.
[29] I. Gonzalez-Prieto, M. J. Duran, J. J. Aciego, C. Martin, and F. Barrero, “Model predictive control of six-phase induction motor drives using virtual voltage vectors,” *IEEE Trans. Ind. Electron.*, vol. 65, no. 1, pp. 27–37, Jan. 2018.
[30] J. Rodas et al., “Sequential model predictive torque control for six-phase machines without weighting factors,” *IEEE Open J. Power Electron.*, vol. 6, pp. 802–810, 2025.
[31] P. Maidana et al., “Sequential model predictive torque control with virtual vectors applied to six-phase induction machine,” in *Proc. IEEE Transp. Electrific. Conf. Expo*, 2024, pp. 1–6.

PAOLA MAIDANA received the B.S. degree in electronic engineering and the M.Sc. degree in electronic engineering with an emphasis on power electronics from Facultad de Ingeniería, Universidad Nacional de Asunción (FIUNA), San Lorenzo, Paraguay. She is currently working toward the Ph.D. degree in electronic engineering with Facultad de Ingeniería, FIUNA. Her research interests include advanced control of electrical drives, power electronic converters, and renewable energy. She conducts her research at the Power and Control Systems Laboratory, FIUNA.

CHRISTIAN MEDINA received the B.S. degree in electronic engineering and the M.Sc. degree in electronic engineering with an emphasis on power electronics from Facultad de Ingeniería, Universidad Nacional de Asunción (FIUNA), San Lorenzo, Paraguay. He is currently working toward the Ph.D. degree in electronic engineering with Facultad de Ingeniería, FIUNA. His research interests include power electronic converters, nonlinear control, operation of electrical drives and renewable energy. He conducts his research at the Power and Control Systems Laboratory, FIUNA.

JESÚS DOVAL-GANDOY (Member, IEEE) received the M.S. degree in electrical engineering from the Polytechnic University of Madrid, Madrid, Spain, in 1991, and the Ph.D. degree in electrical engineering from the University of Vigo, Vigo, Spain, in 1999. He is currently a Professor and the Head of the Applied Power Electronics Technology Research Group, University of Vigo. His research focuses on AC power conversion.

JORGE RODAS (Senior Member, IEEE) received the Ph.D. degree in electronic engineering from a Joint University Program between Universidad Nacional de Asunción (UNA), San Lorenzo, Paraguay, and Universidad de Sevilla, Seville, Spain, in 2016. He is currently a Professor and the Research Director with Facultad de Ingenieria, UNA. With more than 165 published papers, his research interests include advanced control applications for power electronic converters, renewable energy systems, and electric motor drives. He was the recipient of the Paraguayan National Science Award. He was the Guest Editor of IEEE JOURNAL OF EMERGING AND SELECTED TOPICS IN POWER ELECTRONICSand an Associate Editor for IEEE ACCESS. He is also a fellow of the Institution of Engineering and Technology, U.K.

OSVALDO GONZALEZ was born in Asunción, Paraguay. He received the B.Eng. degree in electronic engineering from Universidad Nacional de Asunción (UNA), San Lorenzo, Paraguay, in 2014, and the M.Sc. and Ph.D. degrees in power electronics from the Faculty of Engineering, UNA, in 2017 and 2021, respectively. His research focuses on control of multiphase motors. He was the recipient of the Paraguayan National Science Award.

MAGNO AYALA (Member, IEEE) received the B.Eng. degree in electronic engineering from Universidad Nacional de Asunción (UNA), San Lorenzo, Paraguay, in 2014, and the M.Sc. and Ph.D. degrees in power electronics from the Faculty of Engineering, UNA, in 2017 and 2020, respectively. His research focuses on control of multiphase AC machines. He was the recipient of the 2020 Paraguayan National Science Award and in 2021 the Industrial Electronics Society Best Conference Paper Award in 2020.

RAUL GREGOR (Member, IEEE) was born in Asunción, Paraguay, in 1979. He received the engineer degree in electronic engineering from the Catholic University of Asunción, Asunción, Paraguay, in 2005, and the M.Sc. and Ph.D. degrees in electronics, signal processing, and communications from the Higher Technical School of Engineering, University of Seville, Seville, Spain, in 2008 and 2010, respectively. Since 2010, he has been the Head of the Laboratory of Power and Control Systems, Engineering Faculty, National University of Asunción (FIUNA), San Lorenzo, Paraguay. He is currently the Head of the Department of Electronic and Mechatronics Engineering, FIUNA. He ha has authored or coauthored more than 150 technical papers in the field of power electronics and control systems. His research interests include multiphase drives, advanced control of power converter topologies, power quality, renewable energies, modeling, simulation, optimization, and control of power systems, smart metering, smart grids, and predictive control. He was the recipient of the Best Paper Award from the IEEE Transactions on Industrial Electronics, Industrial Electronics Society, in 2010 and the Best Paper Award from IET Electric Power Applications, in 2012. Since 2017, he has led the technology-based company PQEnerSol SRL, developing cutting-edge technology applied to the energy sector.